Phase Transformation in MOCVD Growth of $(Al_xGa_{1-x})_2O_3$ Thin Films

A F M Anhar Uddin Bhuiyan[1], Zixuan Feng[1], Jared M. Johnson[2], Hsien-Lien Huang[2], Jith Sarker[3], Menglin Zhu[2], Md Rezaul Karim[1], Baishakhi Mazumder[3], Jinwoo Hwang[2], and Hongping Zhao[1,2,a)]

[1]*Department of Electrical and Computer Engineering, The Ohio State University, Columbus, OH 43210, USA*

[2]*Department of Materials Science and Engineering, The Ohio State University, Columbus, OH 43210, USA*

[3]*Department of Materials Design and Innovation, University at Buffalo, Buffalo, New York 14260, USA*

[a)]Corresponding author Email: zhao.2592@osu.edu

This paper investigated the growth of $(Al_xGa_{1-x})_2O_3$ thin films on semi-insulating (010) Ga_2O_3 substrates over the entire Al composition range ($0< x \leq 100\%$) via metalorganic chemical vapor deposition (MOCVD). For the Al composition $x < 27\%$, high quality single phase β-$(Al_xGa_{1-x})_2O_3$ was achieved. A mixture of β and γ phases existed in $(Al_xGa_{1-x})_2O_3$ when Al composition ranged between 27% and 40%, whereas single γ-phase was observed for the films with Al composition $x > 40\%$. The transition from β to γ phase in AlGaO alloys was observed from X-ray diffraction spectra. The growth of γ-phase AlGaO with higher Al content was further confirmed via atomic resolution scanning transmission electron microscopy imaging and nanodiffraction. Compositional and statistical analyses performed on data acquired from atom probe tomography provided insight on the local compositional homogeneity in AlGaO films with different Al compositions. For AlGaO with pure β or γ phases, the Al composition distribution showed homogeneity with similar Al composition values as extracted from the X-ray diffraction peak positions. For AlGaO films with mixed β and γ phases, inhomogeneity in Al composition distribution became more obvious in the nm scale. A mechanism was proposed for the observed phase transformation between β and γ phases in MOCVD growth of AlGaO films.

Keywords: Ultra-wide bandgap, β and γ-AlGaO thin films, metalorganic chemical vapor deposition, phase segregation

β-Ga_2O_3 has attracted extensive attention recently as a promising ultrawide bandgap semiconductor material because of its advantages from large bandgap energy (~ 4.8 eV), predicted high breakdown field strength (~ 8 MV/cm), n-type doping capability and the availability of high-quality native substrates [1]. Despite being at an early development stage, β-Ga_2O_3 based devices including lateral [2-4] and vertical [5, 6] field effect transistors, Schottky barrier diodes [7-9] and ultraviolet photodetectors [10] on bulk and epitaxial thin films [11-13] have been conceptually demonstrated.

Ga_2O_3 has five known polymorphs (α, β, γ, δ, ε) with the β phase representing the most stable one, which forms a complex monoclinic lattice [14]. Alloying Ga_2O_3 with Al_2O_3 can expand the energy bandgap of $(Al_xGa_{1-x})_2O_3$ up to 8.8 eV [15], which can provide opportunities for optoelectronics in deep ultraviolet and electronics with even higher critical field strength. In addition, the AlGaO/GaO heterostructures forming a two dimensional electron gas (2DEG) can enable high power and high frequency electronics. As compared to 2DEGs in AlGaN/GaN, electron mobility at AlGaO/GaO interface is predicted to be lower. However, because of its higher critical field strength, AlGaO/GaO field effect transistors can still gain benefits from device miniaturization, potentially exceeding what AlGaN/GaN devices can achieve today. Furthermore, theoretical modeling predicts much higher 2DEG mobility at AlGaO/GaO interfaces than that of the bulk mobility when the charge concentration is high enough with phonon screening effect [16]. Recently, an AlGaO/GaO 2DEG channel in a modulation doped field effect transistor (MODFET) with 2DEG sheet charge density of 2×10^{12} cm^{-2} demonstrated room temperature mobility of 180 $cm^2/V \cdot s$ and low temperature peak mobility of 2790 $cm^2/V \cdot s$ [17,18]. To maximize the device performance provided by GaO and AlGaO, development of high quality AlGaO epitaxy with

varied Al composition and the fundamental understanding of its chemical, structural and electrical properties are important for the research community.

Due to the different ground state crystal structures of thermally-stable monoclinic β-Ga_2O_3 (space group C2/m) and corundum α-Al_2O_3 (space group $R\bar{3}c$), the solubility of Al_2O_3 in β-Ga_2O_3 is expected to be limited [15]. The phase diagram of $(Al_xGa_{1-x})_2O_3$ alloy, mapped at temperatures ranging between 200 and 2200 °C, predicts the existence of stable monoclinic β-phase AlGaO with Al composition up to 67% [19]. First-principle calculations using hybrid density functional theory (DFT) indicate the monoclinic β-phase AlGaO remains energetically preferable up to Al composition of 71%, whereas the corundum α-phase is preferred at higher Al composition [15]. However, experimental demonstration of phase stability in $(Al_xGa_{1-x})_2O_3$ alloy with a complete mapping of Al composition is still lacking.

Prior efforts on the growth of $(Al_xGa_{1-x})_2O_3$ include β-$(Al_xGa_{1-x})_2O_3$ growth via MBE [20] and MOCVD [21,22] with verified Al composition up to ~20% and 27%, respectively, MBE growth of defective-spinel-structured γ-$(Al_xGa_{1-x})_2O_3$ [23] with the entire range of Al compositions on closely lattice-matched $MgAl_2O_4$ substrates, mist chemical vapor deposition growth of corundum structured α-$(Al_xGa_{1-x})_2O_3$ with Al composition up to 81% [24] and orthorhombic structured ε-$(Al_xGa_{1-x})_2O_3$ with Al composition up to 39.5% [25]. The growth studies of β-$(Al_xGa_{1-x})_2O_3$ films indicate the appearance of phase segregation in the (010) AlGaO layer when targeting for Al compositions > 27% either by MBE [20] or MOCVD [21]. On the other hand, previous studies on pulsed laser deposition (PLD) of $(Al_xGa_{1-x})_2O_3$ films on cubic MgO substrates show the existence of a phase transition from β to γ when Al composition is approximately 50% [26]. PLD growth of γ-Al_2O_3 films on (010) β-Ga_2O_3 substrates shows similar cubic close-packing oxygen sublattices [27]. These prior studies indicate that the γ-$(Al_xGa_{1-x})_2O_3$

may be stabilized with relatively high Al compositions. The physical mechanisms associated with the phase segregation in β-$(Al_xGa_{1-x})_2O_3$ films with relatively high Al composition is not understood.

In this work, we systematically investigated MOCVD growth of $(Al_xGa_{1-x})_2O_3$ thin films with Al composition ranging from 0 to 100 % to understand its phase stability. Comprehensive characterization via X-ray diffraction (XRD), atomic scale high resolution STEM imaging and STEM nanodiffraction showed that the phase of $(Al_xGa_{1-x})_2O_3$ thin films transforms from the monoclinic β-phase to the defective-spinel-structured γ-phase as Al composition increases. The dependence of the surface morphologies of AlGaO thin films on Al composition was studied via field emission scanning electron microscopy (FESEM) and atomic force microscopy (AFM). Chemical homogeneity in AlGaO thin films as a function of Al composition was probed by atom probe tomography (APT).

The $(Al_xGa_{1-x})_2O_3$ thin films were grown on Fe-doped semi-insulating (010) β-Ga_2O_3 substrates acquired commercially from Novel Crystal Technology, Inc. All substrates were in-situ annealed at 920 °C for 30 minutes under O_2 atmosphere prior epi-growth. Triethylgallium (TEGa), Trimethylaluminum (TMAl) and pure O_2 were used as Ga, Al and O precursors, respectively. Argon (Ar) was used as a carrier gas. All films were grown at 880 °C with chamber pressure of 20 Torr. The molar flow rate ratio of [TMAl]/[TMAl+TEGa] was varied between 2.35% and 100%. The film growth rate ranged between 0.82 μm/hr and 1.47 μm/hr. The crystalline quality and Al composition of $(Al_xGa_{1-x})_2O_3$ thin films were characterized by high resolution XRD spectroscopy taken with a Bruker D8 Discover. Representative thin film morphologies were characterized by FESEM (FEI Helios 600) and AFM (Bruker AXS Dimension Icon). For APT sample preparation, focused ion beam (FIB) techniques were used. A 50 nm thick nickel (Ni) layer was deposited on

top via electron beam evaporation to protect the surface from possible ion beam damage. A pulsed laser assisted CAMECA LEAP 5000X HR was used for APT analysis. A Thermo Fisher Scientific Titan STEM, operating at 300 kV, was used to perform high-angle annular dark-field (HAADF) STEM imaging and nanodiffraction.

Figure 1 shows the plot of the XRD ω-2θ scanning spectra for $(Al_xGa_{1-x})_2O_3$ thin films grown with systematic tuning of [TMAl]/[TMAl+TEGa] molar flow rate ratio between 2.35% and 100%, targeting for different Al compositions. Besides the (020) XRD diffraction peak at 2θ = 60.9° from β-Ga_2O_3 substrate, the peak from the epi-grown $(Al_xGa_{1-x})_2O_3$ thin films showed systematic shift toward higher 2θ angles with increasing Al composition. The XRD diffraction peaks corresponded to β-phase $(Al_xGa_{1-x})_2O_3$ with lower Al compositions. For the extraction of Al compositions, we assumed the epi-films were strained as the $(Al_xGa_{1-x})_2O_3$ film thicknesses ranged ~100-200 nm [28]. One exception was from the Al_2O_3 sample, which had a thickness of ~553 nm. Through increasing the TMAl molar flow rate, up to 40% of Al incorporation into $(Al_xGa_{1-x})_2O_3$ films with (020) reflection in β-phase can be identified. However, for β-$(Al_xGa_{1-x})_2O_3$ with Al composition between 27% and 40%, a second XRD peak appeared at 2θ ~ 65.1°, which was identified as the γ-phase. As the TMAl molar flow rate further increased, the γ-phase peak intensity increased with the suppression of the (020) β-phase reflection peak. The XRD peak at 2θ ~ 65.1° was identified as the γ-$(Al_xGa_{1-x})_2O_3$ (440) with 39% of Al composition. As the [TMAl]/[TMAl+TEGa] molar flow rate ratio continued to increase, the pure γ-phase (440) peak position exhibited a monotonic shift from 39% up to 100%. The Al compositions in γ-phase AlGaO were calculated by using Vegard's law from the XRD diffraction peak positions of (440) oriented γ-Ga_2O_3 [29, 30] and γ-Al_2O_3 [27]. As shown in Fig. 1, in both β- and γ- phase zones, as the Al composition increased, the XRD diffraction peak intensities for (020) β-AlGaO peaks and (440) γ-AlGaO peaks decreased as

the corresponding Al composition increased. There existed a transition region where both β- and γ- phases were present. The phase transition only occurred when β-phase Al composition was higher than 27%. With lower Al composition, β-$(Al_xGa_{1-x})_2O_3$ is a preferred formation phase on (010) growth surface. As the Al composition increases, the accumulated strain in the grown film causes the competition between β and γ phases. From our studies, the competing γ-phase $(Al_xGa_{1-x})_2O_3$ appeared with Al composition of ~ 39%. It is worthwhile to note that comparatively lower X-ray scattering factor of Al than that of Ga can partially contribute to the reduction of the peak intensity with increasing of Al composition [31]. However, the main cause of the XRD peak intensity reduction is believed to be the degradation of the crystalline quality of $(Al_xGa_{1-x})_2O_3$ films when Al composition increases.

Table 1 lists the series of $(Al_xGa_{1-x})_2O_3$ samples with different targeted Al compositions. The table summarized the [TMAl]/[TMAl+TEGa] molar flow rate ratio, Al compositions extracted from X-ray diffraction peak positions and atom probe tomography, film thickness and growth rate for these selected samples. The film thicknesses were estimated by characterizing $(Al_xGa_{1-x})_2O_3$ films grown on sapphire substrates, which were co-loaded with (010) Ga_2O_3 substrates during the growth. For the $(Al_xGa_{1-x})_2O_3$ samples, the growth rate increased from 0.82 to 1.47 μm/hr as the [TMAl]/[TMAl+TEGa] molar flow rate ratio increased from 2.35% to 33.80%. Under the studied growth conditions, the Al incorporation efficiency increased as the [TMAl]/[TMAl+TEGa] molar flow rate ratio increased. This indicates that Al adatoms serve as more efficient nucleation sites as compared to Ga adatoms. This is similar to the "surface site-blocking effect" in MOVPE growth of AlGaN [32]. Note that for the two Al_2O_3 samples (Sample 10 and 11) with different thicknesses, the XRD peak for Sample 10 showed a slight shift due to the existence of strain in a relatively thin film (Fig. 1).

The crystal structures of $(Al_xGa_{1-x})_2O_3$ films grown on β-Ga_2O_3 substrates were investigated using STEM imaging and nanodiffraction to confirm the occurrence of the γ-phase at high Al compositions. Figs. 2(a) and 2(c) show the cross-sectional STEM images of the γ-$(Al_{0.90}Ga_{0.10})_2O_3$ and γ-Al_2O_3 films, respectively. In both images, the contrast at the interface indicated strain produced from the structural difference between the film and the substrate, while the intensity variation observed in the film displayed non-uniform growth. Insets in the images were the nanodiffraction patterns from the (010) β-Ga_2O_3 substrate. Nanodiffraction patterns acquired from the films displayed the anticipated defective-spinel-structured γ-phase, oriented in the (110) [Figs. 2(b) and 2(d)], confirming the γ-phase growth of the two films.

For (010) AlGaO films with medium Al compositions, both a β-phase rotation and a γ-phase transformation were observed, suggesting a correlation between the developing structures. Figure 3(a) shows an atomic resolution HAADF STEM image of an $(Al_{0.4}Ga_{0.6})_2O_3$ film with three featured regions: (b) (010) β-$(Al_{0.4}Ga_{0.6})_2O_3$, (c) $(\bar{2}01)$ β-$(Al_{0.4}Ga_{0.6})_2O_3$, and (d) (110) γ-$(Al_{0.39}Ga_{0.61})_2O_3$. First, the successful growth of (010) β-$(Al_{0.4}Ga_{0.6})_2O_3$, marked as (b) and shown in Fig. 3(b), displays dark contrast due to the incorporated Al and is oriented along the $[001]_m$ imaging direction of the β-phase, exhibiting its (010) growth continued from the β-Ga_2O_3 substrate. Succeeding the ~ 6 nm thick initial (010) β-$(Al_{0.4}Ga_{0.6})_2O_3$, two distinct structures were observed, one resulting from a rotation and the other from a phase transformation. Figure 3(c) shows the 90° rotation of the (010) β-$(Al_{0.4}Ga_{0.6})_2O_3$ film, producing the $[0\bar{1}0]_m$ imaging orientation of the β-phase and in this case, (001) growth. Additionally, near this region, instead of a rotation, a phase transformation occurs, which results in (110) γ-$(Al_{0.39}Ga_{0.61})_2O_3$ as shown in Fig. 3(d). At this Al composition, the crystal structure is prone to both a 90° rotation of the (010) β-$(Al_{0.4}Ga_{0.6})_2O_3$ film and a complete phase transformation to (110) γ-$(Al_{0.39}Ga_{0.61})_2O_3$, most certainly caused by the

strain from the Al incorporation. Furthermore, this result also suggested a correlation between the two structures, which can be explained by their oxygen sublattice similarities. The relatively small mismatch in their oxygen sublattices signifies the ability to readily transition between the two structures depending on the local Al distribution. Previously, PLD growth of (110) γ-Al_2O_3 on (010) β-Ga_2O_3 suggests the similarity of the oxygen sublattices between them to explain the growth of (110) γ-Al_2O_3 [27]. Here, we observed a strain induced rotation in epitaxial (010) β-$(Al_xGa_{1-x})_2O_3$, which promoted the subsequent growth of (110) γ-$(Al_xGa_{1-x})_2O_3$.

Note that the strain accumulated in the epitaxial films is related to the film thickness. As demonstrated in our previous studies [21], with relatively thin layer, it is feasible to grow phase pure β-AlGaO with relatively high Al composition. About 10 nm of pure β-$Al_{0.4}Ga_{0.6}O$ superlattice structure [21], and 30-40 nm pure β-$Al_{0.26}Ga_{0.74}O$ films [22] were demonstrated.

To investigate the dependence of the surface morphologies of AlGaO films on Al composition and phase transformation, a series of samples were characterized by both SEM and AFM imaging. Figures 4(a)-(c) represent the FESEM images of $(Al_xGa_{1-x})_2O_3$ thin films with Al composition of 10% (pure β-phase), 27% (β-phase, dominant) plus 39% (γ-phase) and 39% (pure γ-phase), respectively. Smooth and featureless surface morphology was observed for the β-$(Al_{0.1}Ga_{0.9})_2O_3$ thin film [Fig. 4(a)]. As the Al composition increased, as shown in Fig. 4(b), the competition between β- and γ- phases led to the increase of surface roughness with visible grains. For the pure γ-$(Al_{0.39}Ga_{0.61})_2O_3$ thin film, the uniformity and surface smoothness restored. The AFM images with scanning area of 5 μm x 5 μm for the same samples are shown in Figs. 4(d)-(f). As the β-phase Al composition increased from 10% to 27%, the surface RMS roughness increased from 0.36 nm [Fig. 4(d)] to 1.26 nm [Fig. 4(e)]. With further increase of Al incorporation, the surface RMS roughness reduced to 0.63 nm [Fig. 4(f)].

Figures 5(a)-(c) shows the AFM scanning images (5 μm x 5 μm) of γ-$(Al_xGa_{1-x})_2O_3$ films with Al composition of 57%, 61% and 100%, respectively. With increasing Al composition from 39% to 61%, the surface RMS roughness values increased monotonically from 0.63 nm [Fig. 4(f)] to 2.04 nm [Figs. 5(a) and 5(b)]. For the 100% Al composition sample with film thickness of ~553 nm, the surface RMS roughness significantly increased to 15.4 nm as shown in Fig 5(c).

To investigate and understand the structural-chemical evolution with different Al content due to the transformation from β-phase to γ-phase, three-dimensional (3D) atom probe tomography (APT) was performed. Figure 6 shows the 3D elemental distribution of an $(Al_xGa_{1-x})_2O_3$ sample grown with the designed Al compositions between 10% and 100% with each sub-layer thickness of 20 nm. The Al and Ga atoms were represented by red and blue dots, respectively. The increase of the density of red dots indicated the increase of the Al compositions as the growth proceeds. The Al compositions in each layer measured from APT found to be in a good agreement with the targeted compositions determined from the X-ray diffraction peaks.

In order to investigate the variation in alloy homogeneity and the compositional segregations with increasing Al incorporation, lateral chemistry map of Al:O and frequency distribution analysis (FDA) of each layer of the thin film were performed. Figure 7 shows the 2D Al/O ratio maps representing the in-plane Al/O distribution for different layers of $(Al_xGa_{1-x})_2O_3$ with different Al contents. Analysis volume with 80 nm of diameter and 4 nm of thickness were selected from each layer for the investigation of alloy homogeneity. At low Al compositions (x = 10% to 20%), the $(Al_xGa_{1-x})_2O_3$ layers were found to be homogeneous with Al distributed randomly as evidenced by the small variations in Al/O ratio in Figs. 7(a) and 7(b). The Ga atoms can easily drift during growth because of its higher adatom mobility which can be accountable for the smaller compositional variation at lower Al content [33]. However, with the increase of the Al

composition, x = 30% (β) to 40% (β) along with 39% (γ-phase), compositional segregation started as shown by the large lateral variation in Al/O ratio in Figs. 7(c) and 7(d). These data represents chemical heterogeneity during the co-existence of both β and γ phases. The lower adatom mobility of Al due to the strong bonding with oxygen can contribute to the compositional fluctuation at higher Al content [33]. As the Al content continues to increase (x = 39% to 61%), lateral deviation in Al/O ratio decreased as shown in Figs. 7(e), 7(f) and 7(g), indicating the beginning of random elemental distribution. This phenomenon can be attributed to the existence of new chemically homogeneous layers of $(Al_xGa_{1-x})_2O_3$. At very high Al content (x = 90% and 100%), variation in Al/O ratio is negligible as evidenced by Figs. 7(h) and 7(i), demonstrating nearly homogeneous layer with uniform Al distribution. This is an indication of the transformation of a new chemical γ-phase from β-phase.

To statistically investigate the inhomogeneity, the Al distributions within sub-layers with different Al compositions were further studied by frequency distribution analysis as shown in Figure 8. The deviation of the observed elemental distribution from that of a binomial fitting indicated chemical inhomogeneity in the layer. For pure β-$(Al_xGa_{1-x})_2O_3$ with Al content x = 10%, the observed Al distribution closely resembled a binomial distribution with a lower Pearson coefficient, μ and higher P value, indicating Al was randomly distributed in the layer [Fig. 8(a)]. The Pearson coefficient, μ approaching 1 implies the presence of elemental segregation and lower P-value means high confidence level during the null hypothesis testing [34]. As the Al composition increased, the observed Al distribution started to deviate from the binomial distribution, implying the increase of inhomogeneity as shown in Fig. 8(b) for $(Al_xGa_{1-x})_2O_3$ sub-layer with x = 40% (β-phase) + 39% (γ-phase). The observed Al distribution deviated considerably from binomial one with higher μ values, confirming Al segregation in the layer due to the co-existence of β- and γ-

phases. At high Al composition (x = 90%), the observed Al distribution fitted with that of the expected binomial distribution with a low μ value, indicating Al was distributed randomly along the plane and the layer homogeneity re-established as illustrated in Fig. 8(c). This phenomenon also suggests the appearance of a new chemical structure γ-$(Al_xGa_{1-x})_2O_3$ at high Al composition.

In summary, phase stability and phase transformation in MOCVD grown $(Al_xGa_{1-x})_2O_3$ thin films were investigated covering the entire Al composition range. Pure β-$(Al_xGa_{1-x})_2O_3$ thin films with high crystalline quality and homogeneity were confirmed with x<27%. The transformation from β- to γ- phase was observed for x>27%. The mixture and competition between β- and γ-phases lead to domain formation and surface roughness, associated with heterogeneity of Al distribution. Pure γ-$(Al_xGa_{1-x})_2O_3$ thin films with smooth surface and good homogeneity were achieved with 39%<x<100%. The comprehensive characterization suggests that strain caused by increased Al incorporation induces the rotation of β-phase AlGaO domains and promotes the formation of γ-phase AlGaO. Additionally, the existence of both structures and their frequent transitions in $(Al_{0.4}Ga_{0.6})_2O_3$ films are attributed to their nearly identical oxygen sublattices. Understanding of the phase transformation mechanism in MOCVD growth of $(Al_xGa_{1-x})_2O_3$ thin films on (010) Ga_2O_3 substrates will provide guidance for potential strategies to develop phase pure $(Al_xGa_{1-x})_2O_3$ with desired Al compositions, which is critical for both electronic and optoelectronic device designs.

Acknowledgements

The authors acknowledge the funding support from the Air Force Office of Scientific Research FA9550-18-1-0479 (AFOSR, Dr. Ali Sayir). Feng and Zhao also acknowledge partial support from the National Science Foundation (1810041).

References:

1. M. Higashiwaki and G. H. Jessen, Appl. Phys. Lett. 112, 060401 (2018).
2. Z. Xia, H. Xue, C. Joishi, J. McGlone , N. K. Kalarickal, S. H. Sohel, M. Brenner, A. Arehart, S. Ringel, S. Lodha, W. Lu, and S. Rajan, IEEE Electron Device Lett. 40, 1052 (2019).
3. M. Higashiwaki, K. Sasaki, A. Kuramata, T. Masui, and S. Yamakoshi, Appl. Phys. Lett. 100, 013504 (2012).
4. J. Green, K. D. Chabak, E. R. Heller, R. C. Fitch, Jr., M. Baldini, A. Fiedler, K. Irmscher, G. Wagner, Z. Galazka, S. E. Tetlak, A. Crespo, K. Leedy, and G. H. Jessen, IEEE Electron Dev. Lett. 37, 902 (2016).
5. M. H. Wong, K. Goto, H. Murakami, Y. Kumagai, and M. Higashiwaki, IEEE Electron Device Lett. 40, 3 (2019).
6. Z. Hu, K. Nomoto, W. Li, N. Tanen, K. Sasaki, A. Kuramata, T. Nakamura, D. Jena and H. G. Xing; IEEE Electr. Device L. 39, 869 (2018).
7. K. Konishi, K. Goto, H. Murakami, Y. Kumagai, A. Kuramata, S. Yamakoshi, and M. Higashiwaki, Appl. Phys. Lett. 110, 103506 (2017).
8. J. Yang, F. Ren, M. Tadjer, S. J. Pearton, and A. Kuramata, ECS J. Solid State Sci. Technol. 7, Q92 (2018).
9. C. Joishi, S. Rafique, Z. Xia, L. Han, S. Krishnamoorthy, Y. Zhang, S. Lodha, H. Zhao, and S. Rajan, Appl. Phys. Express 11, 031101 (2018)
10. T. Oshima, T. Okuno, N. Arai, N. Suzuki, S. Ohira, and S. Fujita, Appl. Phys. Express 1, 011202 (2008).
11. Z. Feng, A F M Anhar Uddin Bhuiyan, M. R. Karim, and H. Zhao, Appl. Phys. Lett. 114, 250601 (2019).
12. S. Rafique, L. Han, M. J. Tadjer, J. A. Freitas Jr, N. A. Mahadik, and H. Zhao, Appl. Phys. Lett. 108, 182105 (2016).
13. H. Okumura, M. Kita, K. Sasaki, A. Kuramata, M. Higashiwaki, and J. S. Speck, Appl. Phys. Express 7, 095501 (2014).
14. R. Roy, V. G. Hill and E. F. Osborn, J. Am. Chem. Soc. 74, 719 (1952).
15. H. Peelaers, J. B. Varley, J. S. Speck, and C. G. Van de Walle, Appl. Phys. Lett. 112, 242101 (2018).
16. K. Ghosh and U. Singisetti, J. Mater. Res. 32, 4142 (2017).
17. Y. Zhang, A. Neal, Z. Xia, C. Joishi, J. M. Johnson, Y. Zheng, S. Bajaj, M. Brenner, D. Dorsey, K. Chabak, G. Jessen, J. Hwang, S. Mou, J. P. Heremans, and S. Rajan, Appl. Phys. Letts. 112, 173502 (2018).
18. S. Krishnamoorthy, Z. Xia, C. Joishi, Y. Zhang, J. McGlone, J. Johnson, M. Brenner, A. R. Arehart, J. Hwang, S. Lodha, and S. Rajan, Appl. Phys. Lett. 111, 023502 (2017)
19. V.G. Hill, R. Roy, and E.F. Osborn, J. Am. Ceram. Soc. 35, 135 (1952).
20. P. Vogt, A. Mauze, F. Wu, B. Bonef, and J. S. Speck, Appl. Phys. Express 11, 115503 (2018).

21. A F M Anhar Uddin Bhuiyan, Z. Feng, J. M. Johnson, Z. Chen, H.-L. Huang, J. Hwang, and H. Zhao, Appl. Phys. Lett. 115, 120602 (2019).
22. P. Ranga, A. Rishinaramangalam, J. Varley, A. Bhattacharyya, D. Feezell, and S. Krishnamoorthy, Appl. Phys. Express 12, 111004 (2019).
23. T. Oshima, Y. Kato, M. Oda, T. Hitora, and M. Kasu, Appl. Phys. Express 10, 051104 (2017).
24. H. Ito, K. Kaneko and S. Fujita, Jpn. J. Appl. Phys. 51, 100207 (2012).
25. D. Tahara, H. Nishinaka, S. Morimoto, and M. Yoshimoto, Appl. Phys. Lett. 112, 152102 (2018).
26. C. Kranert, M. Jenderka, J. Lenzner, M. Lorenz, H. von Wenckstern, R. Schmidt-Grund, and M. Grundmann, J. Appl. Phys. 117, 125703 (2015).
27. M. Hattori, T. Oshima, R. Wakabayashi, K. Yoshimatsu, K. Sasaki, T. Masui, A. Kuramata, S. Yamakoshi, K. Horiba, H. Kumigashira, and A. Ohtomo, Jpn. J. Appl. Phys. 55, 1202B6 (2016).
28. Y. Oshima, E. Ahmadi, S. C. Badescu, F. Wu, and J. S. Speck, Appl. Phys. Express 9, 061102 (2016).
29. C.-C Huang and C.-S Yeh, New J. Chem. 34, 103 (2010).
30. Y. Hou, L. Wu, X. Wang, Z. Ding, Z. Li, X. Fu, J. Catal. 250, 12 (2007).
31. T. Oshima, T. Okuno, N. Arai, Y. Kobayashi, and S. Fujita, Jpn. J. Appl. Phys. 48, 070202 (2009).
32. J. Han, J. J. Figiel, M. H. Crawford, M. A. Banas, M. E. Bartram, R. M. Biefeld, Y. K. Song, and A. V. Nurmikko, J. Cryst. Growth 195, 291 (1998).
33. B. Mazumder, J. Sarker, Y. Zhang, J. M. Johnson, M. Zhu, S. Rajan, and Jinwoo Hwang, Appl. Phys. Lett. 115, 132105 (2019).
34. A. Devaraj, M. Gu, R. Colby, P. Yan, C. M. Wang, J. M. Zheng, J. Xiao, A. Genc, J. G. Zhang, I. Belharouak, D. Wang, K. Amine and S. Thevuthasan, Nature Communications, 6, (2018).

Table Caption

Table 1. Summary of the series of $(Al_xGa_{1-x})_2O_3$ samples grown at different [TMAl]/[TMAl + TEGa] molar flow rate ratio, with film thicknesses, growth rates, and extracted Al compositions from XRD and APT characterization.

Figure Caption

Figure 1 XRD pattern for β-$(Al_xGa_{1-x})_2O_3$ and γ-$(Al_yGa_{1-y})_2O_3$ thin films grown on (010) β-Ga_2O_3 substrates with different Al compositions. The blue vertical dashed lines represent the 2θ peak positions for β-Ga_2O_3 (020) and β-Al_2O_3 (020) whereas red dashed lines represent the γ-Ga_2O_3 (440) and γ-Al_2O_3 (440) peak positions. XRD peaks for β-$(Al_xGa_{1-x})_2O_3$ (020) films with x = 10%, 15%, 18%, 27% and 40% and γ-$(Al_yGa_{1-y})_2O_3$ (440) films with y = 39%, 57%, 61%, 90% and 100% were identified.

Figure 2 STEM imaging and nanodiffraction of γ-$(Al_{0.90}Ga_{0.10})_2O_3$ and γ-Al_2O_3 films. Cross-sectional high resolution HAADF STEM images of the (a) γ-$(Al_{0.90}Ga_{0.10})_2O_3$ and (c) γ-Al_2O_3 films grown on (010) β-Ga_2O_3 substrate with (inset) nanodiffraction from the substrate presenting the pure monoclinic phase. Nanodiffraction from (b) γ-$(Al_{0.90}Ga_{0.10})_2O_3$ and (d) γ-Al_2O_3 films reveal the (110) γ-phase.

Figure 3 Atomic resolution HAADF STEM images of the $(Al_{0.40}Ga_{0.60})_2O_3$ film grown on β-Ga_2O_3 substrate. (a) The first 12 nm of the $(Al_{0.40}Ga_{0.60})_2O_3$ film demonstrating three distinct growth structures. (b) (010) β-$(Al_{0.40}Ga_{0.60})_2O_3$ growth with the model orientated along the $[001]_m$ imaging direction. (c) $(\bar{0}01)$ β-$(Al_{0.4}Ga_{0.6})_2O_3$ growth displaying a 90° rotation of the (010) β-$(Al_{0.40}Ga_{0.60})_2O_3$ and a model oriented along the corresponding $[0\bar{1}0]_m$ imaging direction. (d) (110) γ-$(Al_{0.39}Ga_{0.61})_2O_3$ phase transformation region with a model of [110] γ-Al_2O_3.

Figure 4 Surface view FESEM images of β-$(Al_xGa_{1-x})_2O_3$ (109 nm thick), β-$(Al_xGa_{1-x})_2O_3$ plus γ-$(Al_yGa_{1-y})_2O_3$ (113 nm thick) and γ-$(Al_yGa_{1-y})_2O_3$ (150 nm thick) films with (a) x = 10% (β-phase), (b) x = 27% (β-phase) plus y = 39% (γ-phase) and (c) y = 39% (γ-phase), respectively. The corresponding AFM images of (a) β-$(Al_{0.10}Ga_{0.90})_2O_3$ (b) β-$(Al_{0.27}Ga_{0.73})_2O_3$ plus γ-$(Al_{0.39}Ga_{0.61})_2O_3$ (c) γ-$(Al_{0.39}Ga_{0.61})_2O_3$ films. The scan area is 5 x 5 μm^2.

Figure 5 The AFM images of γ-$(Al_xGa_{1-x})_2O_3$ films with (a) x = 57% (150 nm thick), (b) x = 61% (181 nm thick) and (c) x = 100% (553 nm thick) of Al compositions. The scan area is 5 x 5 μm^2.

Figure 6 (a) 3D atomic map of the layered $(Al_xGa_{1-x})_2O_3/Ga_2O_3$ heterostructure with varying Al composition. Only Al and Ga atoms are shown for clarity; (b) Schematic diagram of the layered $(Al_xGa_{1-x})_2O_3/Ga_2O_3$ heterostructure in (a).

Figure 7 2D atomic distribution showing Al/O concentration ratio in lateral plane of each layer with Al compositions of (a) 10% (β), (b) 20% (β), (c) 27% (β) + 39% (γ), (d) 40% (β) + 39% (γ), (e) 39% (γ), (f) 57% (γ), (g) 61% (γ), (h) 90% (γ) and (i) 100% (γ).

Figure 8 Frequency distribution analysis of Al for $(Al_xGa_{1-x})_2O_3$ films with Al compositions of (a) 10% (β-phase), (b) 40% (β-phase) + 39% (γ-phase), (c) 90% (γ-phase) comparing the observed Al distributions with the binomial distribution.

Table 1

Sample	[TMAl]/[TMAl +TEGa] (%)	Al composition (XRD) (%)	Al composition (APT) (%)	Film Thickness (nm)	Growth rate (μm/hr)
1	2.35	10 (β)	10.240 ± 0.88	109	0.82
2	3.82	15 (β)	-	110	0.83
3	5.91	20 (β)	21.665 ± 0.13	110	0.83
4	7.27	27 (β) + 39 (γ)	29.535 ± 0.15	113	0.85
5	10.36	40 (β) + 39 (γ)	40.622 ± 0.18	124	0.93
6	15.73	39 (γ)	47.955 ± 0.21	150	1.13
7	24.04	57 (γ)	51.337 ± 0.22	169	1.27
8	28.79	61 (γ)	60.832 ± 0.26	181	1.36
9	33.80	90 (γ)	81.245 ± 0.39	196	1.47
10	100.00	100 (γ)	98.815 ± 0.34	181	1.09
11	100.00	100 (γ)	-	553	1.11

Figure 1

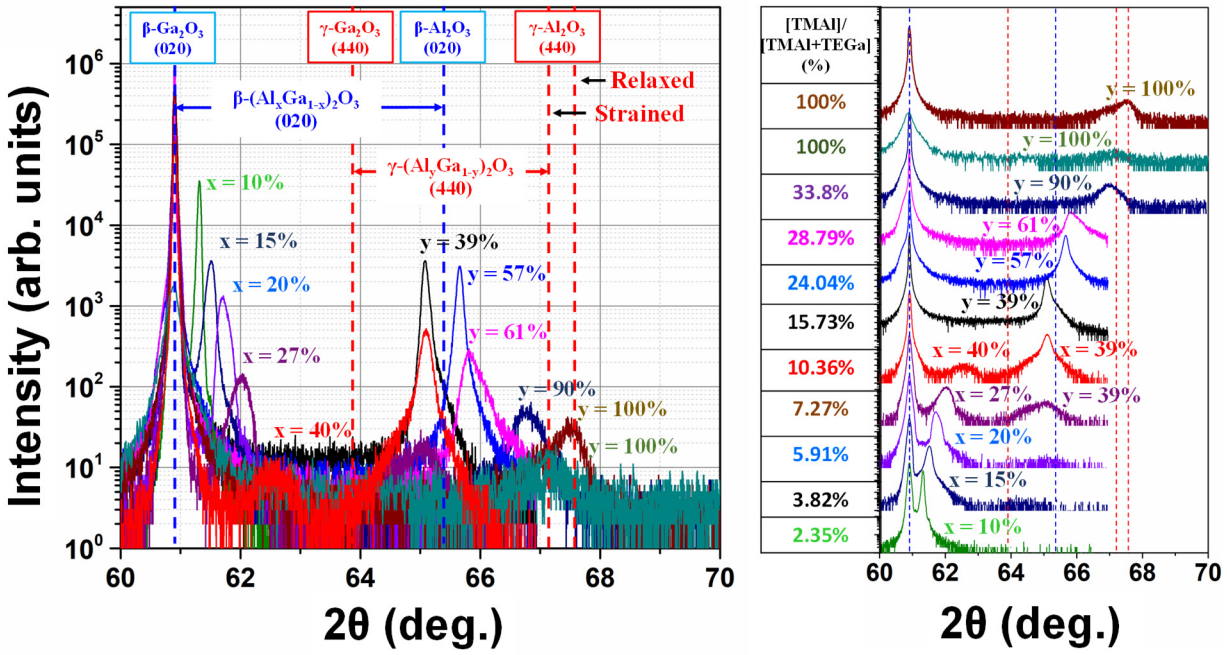
β-Ga2O3 (020)
γ-Ga2O3 (440)
β-Al2O3 (020)
γ-Al2O3 (440)
β-(AlxGa1-x)2O3 (020)
γ-(AlyGa1-y)2O3 (440)
Relaxed
Strained
x = 10%
x = 15%
x = 20%
x = 27%
x = 40%
y = 39%
y = 57%
y = 61%
y = 90%
y = 100%
y = 100%
Intensity (arb. units)
2θ (deg.)
[TMAl]/[TMAl+TEGa] (%)
100%
100%
33.8%
28.79%
24.04%
15.73%
10.36%
7.27%
5.91%
3.82%
2.35%
y = 100%
y = 100%
y = 90%
y = 61%
y = 57%
y = 39%
x = 40%
x = 39%
x = 27%
y = 39%
x = 20%
x = 15%
x = 10%
2θ (deg.)

Figure 2

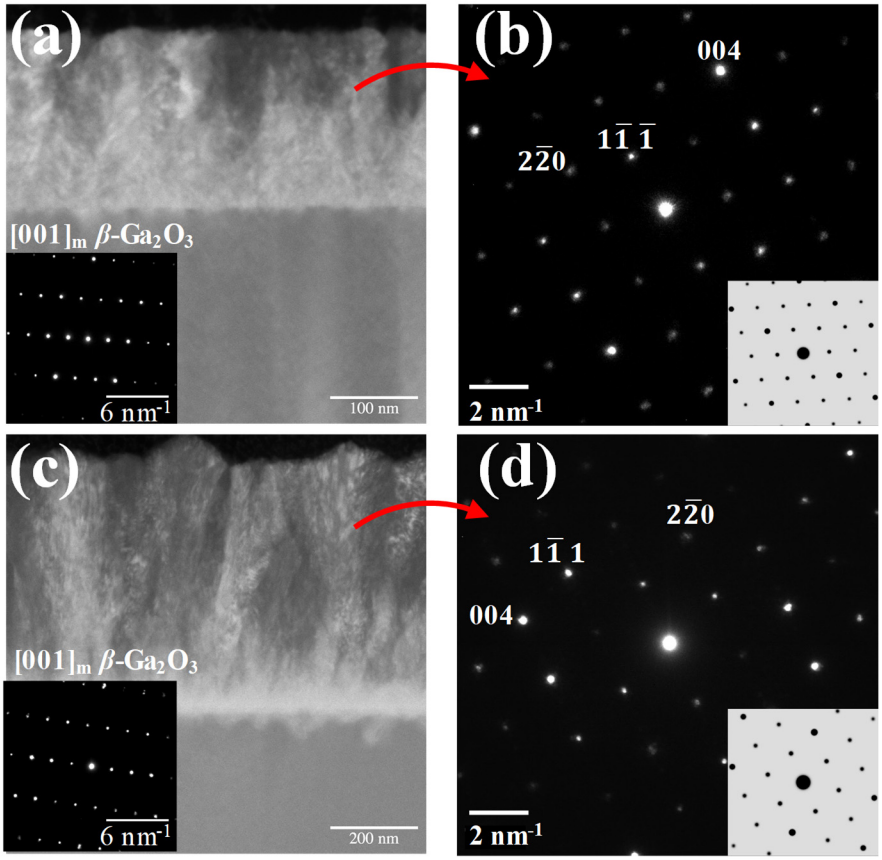
(a)
[001]m β-Ga2O3
6 nm-1
100 nm
(b)
004
1$\bar{1}$ $\bar{1}$
2$\bar{2}$0
2 nm-1
(c)
[001]m β-Ga2O3
6 nm-1
200 nm
(d)
2$\bar{2}$0
1$\bar{1}$ 1
004
2 nm-1

Figure 3

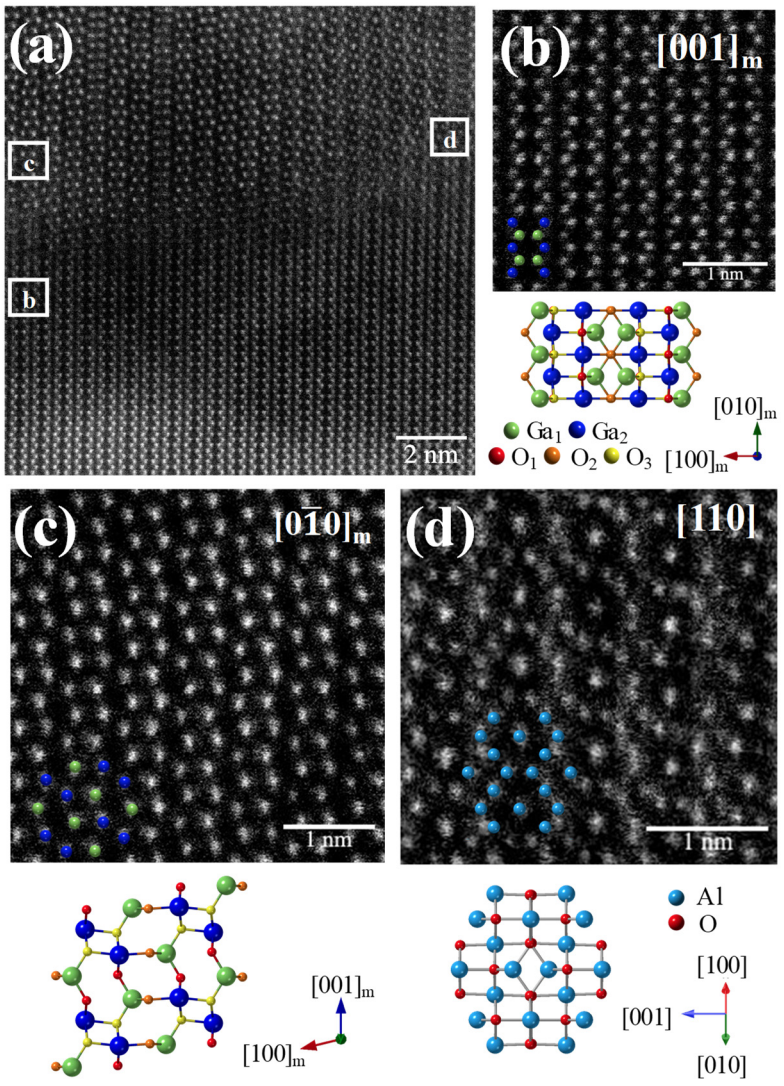
(a)
c
d
b
2 nm
(b)
[001]m
1 nm
[010]m
Ga1 Ga2
O1 O2 O3
[100]m
(c)
[0$\bar{1}$0]m
1 nm
[001]m
[100]m
(d)
[110]
1 nm
Al
O
[100]
[001]
[010]

Figure 4

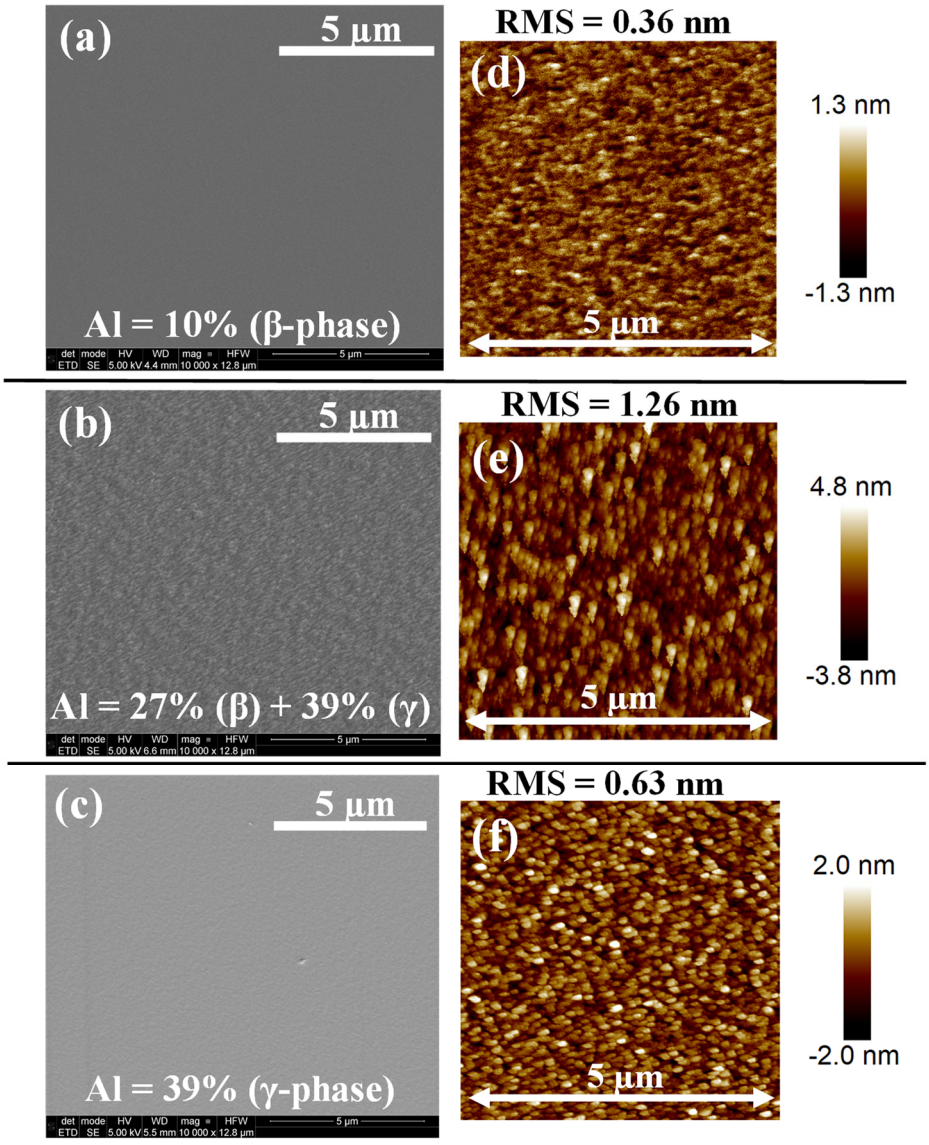
(a)
5 µm
Al = 10% (β-phase)
RMS = 0.36 nm
(d)
5 µm
1.3 nm
-1.3 nm
(b)
5 µm
Al = 27% (β) + 39% (γ)
RMS = 1.26 nm
(e)
5 µm
4.8 nm
-3.8 nm
(c)
5 µm
Al = 39% (γ-phase)
RMS = 0.63 nm
(f)
5 µm
2.0 nm
-2.0 nm

Figure 5

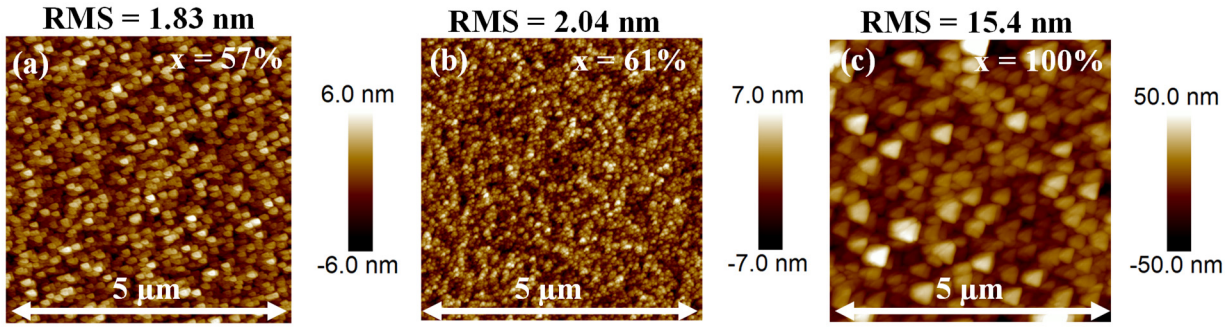
RMS = 1.83 nm
(a)
x = 57%
6.0 nm
-6.0 nm
5 µm
RMS = 2.04 nm
(b)
x = 61%
7.0 nm
-7.0 nm
5 µm
RMS = 15.4 nm
(c)
x = 100%
50.0 nm
-50.0 nm
5 µm

Figure 6

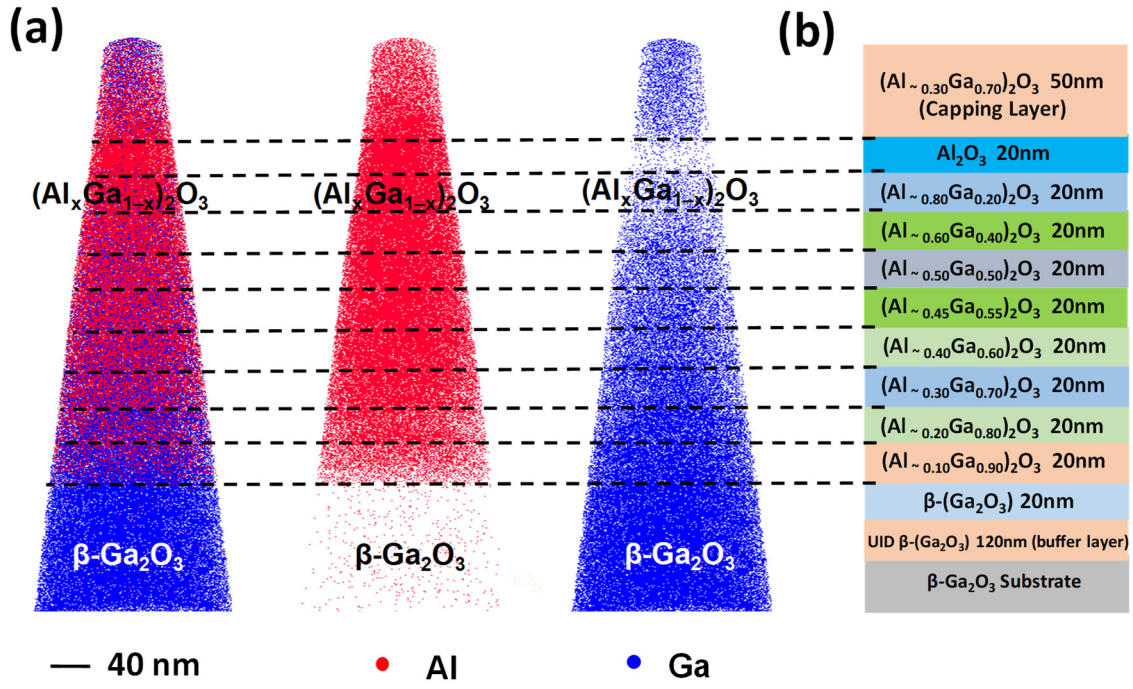
(a)
(b)
$(Al_xGa_{1-x})_2O_3$
$(Al_xGa_{1-x})_2O_3$
$(Al_xGa_{1-x})_2O_3$
β-Ga_2O_3
β-Ga_2O_3
β-Ga_2O_3
— 40 nm
Al
Ga
$(Al_{\sim 0.30}Ga_{0.70})_2O_3$ 50nm (Capping Layer)
Al_2O_3 20nm
$(Al_{\sim 0.80}Ga_{0.20})_2O_3$ 20nm
$(Al_{\sim 0.60}Ga_{0.40})_2O_3$ 20nm
$(Al_{\sim 0.50}Ga_{0.50})_2O_3$ 20nm
$(Al_{\sim 0.45}Ga_{0.55})_2O_3$ 20nm
$(Al_{\sim 0.40}Ga_{0.60})_2O_3$ 20nm
$(Al_{\sim 0.30}Ga_{0.70})_2O_3$ 20nm
$(Al_{\sim 0.20}Ga_{0.80})_2O_3$ 20nm
$(Al_{\sim 0.10}Ga_{0.90})_2O_3$ 20nm
β-(Ga_2O_3) 20nm
UID β-(Ga_2O_3) 120nm (buffer layer)
β-Ga_2O_3 Substrate

Figure 7

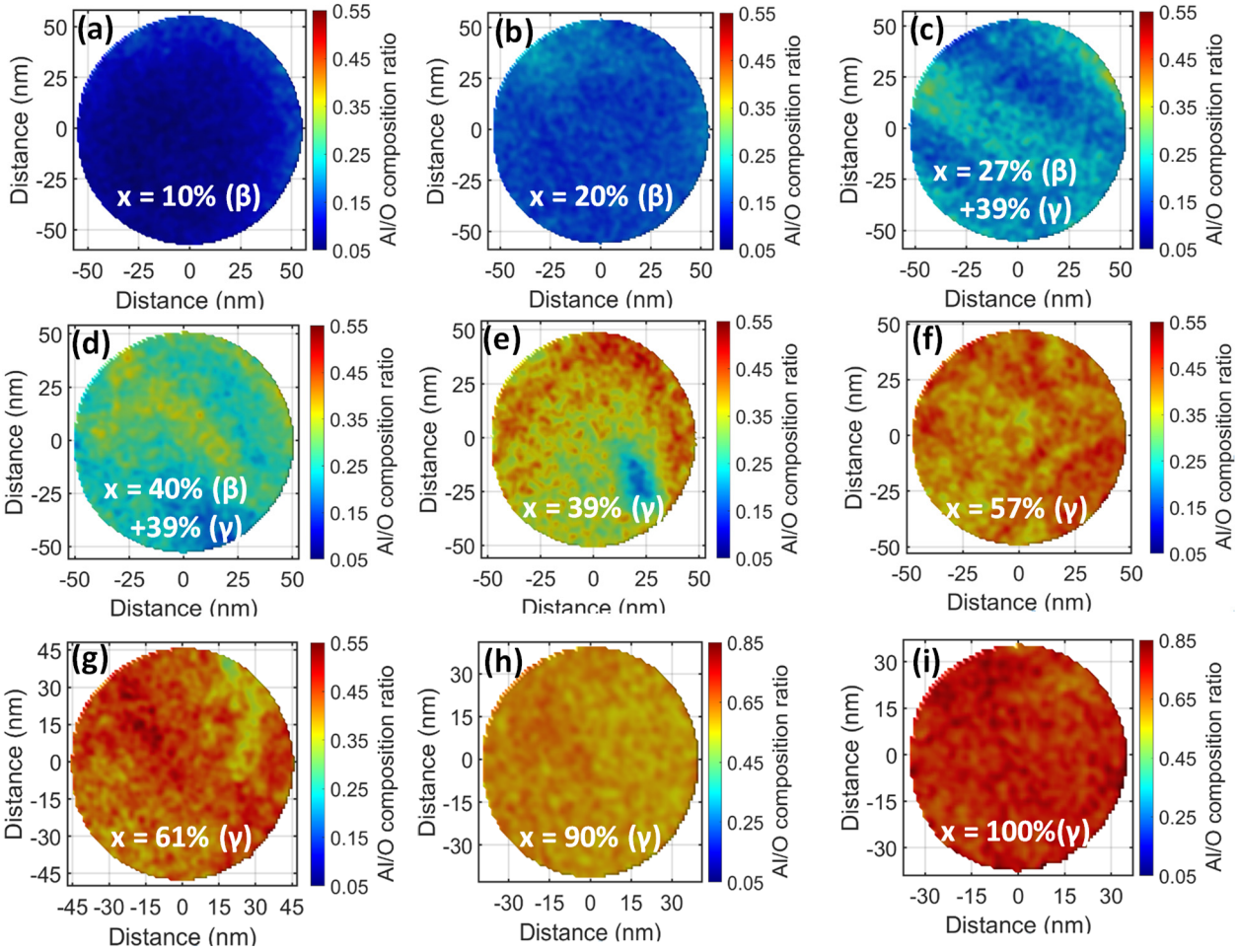
(a)
x = 10% (β)
(b)
x = 20% (β)
(c)
x = 27% (β)
+39% (γ)
(d)
x = 40% (β)
+39% (γ)
(e)
x = 39% (γ)
(f)
x = 57% (γ)
(g)
x = 61% (γ)
(h)
x = 90% (γ)
(i)
x = 100%(γ)
Distance (nm)
Al/O composition ratio

Figure 8

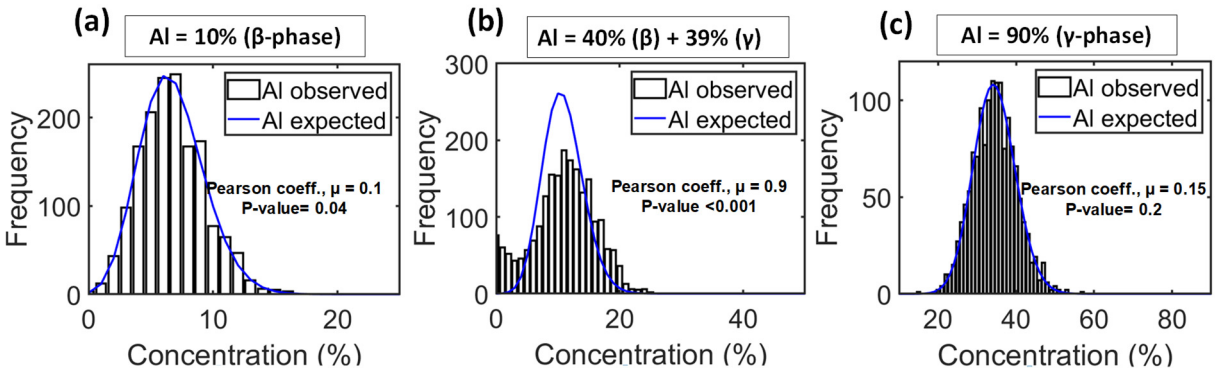
(a)
Al = 10% (β-phase)
Al observed
Al expected
Pearson coeff., μ = 0.1
P-value= 0.04
Frequency
Concentration (%)
(b)
Al = 40% (β) + 39% (γ)
Al observed
Al expected
Pearson coeff., μ = 0.9
P-value <0.001
Frequency
Concentration (%)
(c)
Al = 90% (γ-phase)
Al observed
Al expected
Pearson coeff., μ = 0.15
P-value= 0.2
Frequency
Concentration (%)